nature photonics

Article

https://doi.org/10.1038/s41566-026-02024-9

Phase control of interfering stimulated Raman pathways in the XUV regime

Received: 14 April 2026

Accepted: 4 September 2026

Published online: 09 October 2026

Check for updates

Ulli Eichmann[1] ✉, Stefanos Carlström[1], Serguei Patchkovskii[1], Stefan Eisebitt[1,2], Jan-Erik Rubensson[3], Johan Söderström[3], Jochen Mikosch[4], Enrico Allaria[5], Alexander Brynes[5,8], Carlo Callegari[5], Michele Di Fraia[5,6], Michele Manfredda[5], Nitish Pal[5,9], Giovanni Perosa[5,10], Oksana Plekan[5], Alberto Simoncig[5] & Matthieu Génévriez[7]

Coherent control uses interference between quantum pathways to enhance or suppress transitions to a target quantum state. In stimulated Raman excitation, such control can be achieved through interference between two indistinguishable pathways connecting the same initial and final states, with the relative phase between the pathways modulating the population transfer to the final state. Extending this strategy to the extreme ultraviolet (XUV) and X-ray regimes would enable control of ultrafast electronic dynamics and site-selective core excitations. However, Raman coupling at short wavelengths competes with photoionization and intermediate-state decay, whereas intense fields with stable and adjustable relative phases remain difficult to produce. Here we use two-colour pulses from a seeded coherent free-electron laser to excite helium from its ground state to a bound metastable state via stimulated XUV Raman excitation. We implement phase-coherent control by creating two interfering Raman pathways through the ionization continuum and modulate the transferred population by varying their relative phases. Blocking one pathway removes the modulation, confirming its interferometric origin, and time-dependent Schrödinger equation calculations reproduce the measured phase dependence. Our results establish phase-controlled stimulated Raman excitation in the XUV regime, providing a strategy for the coherent control of atomic and molecular processes at short wavelengths.

With the advent of intense free-electron lasers (FELs) and X-ray free-electron lasers (XFELs)[1], one major goal of the nonlinear optics community has been to replicate fundamental (coherent) nonlinear phenomena of the optical regime and their applications in the extreme ultraviolet (XUV) and X-ray domains. This transfer enables the investigation of time-dependent processes on the femto- and attosecond timescales[2,3] that benefit from the prospective site-sensitivity offered by these wavelength regimes[4].

In this context, the study of the stimulated Raman process[5] has attracted increasing interest. It has been well exploited in the optical regime in applications[6,7] and at the single-atom level. Here, phenomena such as stimulated Raman adiabatic population transfer (STIRAP)[8–11], laser-induced structure in the continuum (LICS)[12–14] and electromagnetically induced transparency (EIT)[15] have been investigated. In the soft X-ray range, the enhanced cross-section due to core–hole resonances has enabled stimulated Raman studies, despite the substantial Auger decay loss channel and the influence of sequential multiphoton processes[16]. Direct observation of stimulated Raman scattering using broadband single XFEL pulses relies on enhancement of the signal due to propagation in dense

A full list of affiliations appears at the end of the paper. ✉e-mail: eichmann@mbi-berlin.de

media[17,18], and the single-atom response has been investigated via photon-recoil imaging[19]. Wavepacket dynamics in molecules[20] and condensed matter[21,22] have been addressed via impulsive stimulated Raman scattering, and a scheme for four-wave mixing in the soft X-ray regime has recently been realized[23]. However, the limited coherence has hampered phase control in the X-ray range.

In the XUV regime the stimulated Raman process has sparked considerable theoretical interest[24–27], but has not yet been demonstrated experimentally. The study of XUV processes with FELs has, so far, extended from the perturbative (multiphoton) regime[28] to the non-perturbative (strong-field) regime[29–31] and, moreover, has covered four-wave mixing[32,33] experiments.

Phase-sensitive coherent control requires establishing two or more interfering pathways between pairs of initial and final states[34]. This type of control scheme has recently been elegantly demonstrated in the XUV regime[35,36]. Robust control needs the two pathways to be well balanced in the number of photons and the cross-sections. A pair of interfering Raman processes through intermediate continuum states is an ideal candidate. Furthermore, this choice dislodges advantageously the XUV photon energies from the excitation energy, thus displacing the background.

In this Article we use the FERMI (Free Electron laser Radiation for Multidisciplinary Investigations) seeded FEL[37] in the two-colour mode to demonstrate the stimulated Raman process in the XUV regime. The coherence of the source enables phase control of the electronic excitation, observed in the interference between two stimulated Raman pathways. Starting from the ground state, we excite the non-dipole-coupled bound metastable state of helium (He) through the continuum using photon energies well above the energy for direct excitation. Detecting metastable atoms, and efficiently discriminating against charged particles, the measurements are unaffected by the strong XUV ionization. Our experiments pave the way for coherent control of site-selective time-dependent processes using short-wavelength radiation.

Results and discussion

Two-photon stimulated Raman transitions in the XUV

The generation of two-colour FEL XUV radiation is shown schematically in Fig. 1a. The photon energies of the two XUV pulses (harmonics H_n and H_m) are multiples of the seed laser photon energy, $E_n = n\hbar\omega_s$ and $E_m = m\hbar\omega_s$, where $\hbar$ is the reduced Planck's constant and ω_s is the angular frequency, and provide the pump and Stokes photon, respectively. Independent of the characteristics of the intermediate state, a two-photon Raman resonance condition is fulfilled if the photon energy difference between the pair of harmonics is equal to the excitation energy of the final state, $E_n - E_m = E_b$, or, in terms of the seed laser photon energy, $(n-m)\hbar\omega_s = E_b$. To realize this scheme, we chose He as the ideal target atom for our purpose. The long-lived metastable He($1s2s\ ^1S$) in the singlet state, which we label as He(2*s*) from here on, has an excitation energy of $E_b = 20.615$ eV (ref. 38) and can be favourably used as the final state. Choosing $n - m = 4$ for the difference of the order of the harmonics, the seed laser photon energy (E_s) needs to be $E_s = \hbar\omega_s = 5.154$ eV, which is within the technically available range[39].

In the experiments we used pairs of harmonics ($H_{m=5,6,7,8}$, $H_{n=m+4}$). These correspond to Stokes photon energies between 25 and 40 eV and pump photon energies between 45 and 60 eV. As visualized in Fig. 1b, they drive the two-photon Raman transition between the ground state He($1s^2$) and the final excited metastable He(2*s*) state via the continuum. We note that, strictly speaking, the continuum is a superposition of bound and continuum states (Supplementary Information, Section 4). As all harmonics are above the single ionization limit of He, $I_{He^+(1s)} = 24.587$ eV, both the pump and the Stokes pulses can ionize He and produce a substantial background of photoelectrons and photoions.

Owing to the small two-photon cross-section compared with the single-photon ionization cross-section, a crucial experimental issue is the sufficiently background-free detection of the final state. This can be achieved with our experimental set-up, displayed in Fig. 1c, which follows the arrangement used in other recent experiments with metastable atoms[19,40,41]. The two-photon Raman excited metastable He atoms travel together with He atoms in the ground state, eventually hitting a (position-sensitive) multi-channel plate (MCP) detector. In contrast to ground-state He atoms with no internal energy, the detection of metastable He(2*s*) is enabled due to its high internal energy. All photoelectrons and ions that are produced in the interaction are deflected perpendicular to the atomic beam by a small static electric field across the interaction volume, and do not reach the detector.

In the first investigation we tuned the two undulator sets to amplify the seventh (first set) and eleventh harmonics (second set), thus generating XUV pulses with energies of 12 and 40 μJ and pulse widths of 61 and 52 fs (full-width at half-maximum (FWHM)), respectively (Methods and Supplementary Information, Sections 1 and 2). The Stokes pulses preceded the pump pulses by 15 fs. The photon energy of the seed laser was tuned such that the difference in the photon energy of the pair of harmonics matches the excitation energy of the metastable state, that is, they were tuned on Raman resonance. The FERMI FEL enables full polarization control of the two pulses separately[42]. We chose to make both harmonics circularly polarized. In this case, the dipole selection rules require that, to drive the two-photon transition, the harmonic pulses be of same handedness (either both right-circularly polarized or both left-circularly polarized).

With both beams right-circularly polarized we measured a time-of-flight spectrum, which shows a strong yield of metastable atoms relative to the background signal (Fig. 1d). To prove the fact that the signal indeed depends on the polarization as expected, we changed the circular polarization of one of the XUV laser pulses to be left-circularly polarized. In this case the Raman process is forbidden according to the dipole selection rules. As displayed in Fig. 1d, the measured He(2*s*) yield drops down to a few percent of the yield obtained when using the correct configuration of polarization. The residual yield can be largely attributed to the imperfect circular polarization. The data clearly show the stimulated Raman process at work.

We measured the He(2*s*) yield for four pairs of circularly polarized harmonics across the Raman resonance by fine-tuning the seed laser photon energy E_s. The results are shown in Fig. 2a. Inspecting the experimental data, we find that in all spectra the lineshapes of the Raman resonance are basically very close to a Gaussian lineshape centred at the predicted transition excitation energy of the metastable state. Furthermore, we observe experimentally that the resonance position does not shift noticeably within the available XUV pulse intensities, and the lineshape remains unaltered. This is somewhat expected, as the Raman cross-sections for continuum transitions are rather low; concomitantly, the Stark shift is minimal, as also confirmed quantitatively in our subsequent calculations.

We solve the time-dependent Schrödinger equation (TDSE) using a single-active-electron approach[43] (Methods; Supplementary Information, Section 3). In Fig. 2b we present the calculated Raman resonances for the harmonic pair (H_7, H_{11}) as a function of the seed laser photon energy using different XUV pulse intensities. As we did not measure absolute yields, the maximum of the theoretical yield was fitted by eye to the experimental result. In the calculation we used the XUV pulse intensities 118 and 984 TW cm^{-2} for the harmonics H_7 and H_{11}, respectively, which were determined from experimental parameters and the pulse duration (Methods). We performed three additional calculations, halving the intensities in each case. Only at the highest intensities (black curve in Fig. 2b) do we observe a slight Stark shift. For lower intensities, we obtain no resonance shift and Gaussian-like resonance profiles, with a fixed width for all intensities below 30 and 246 TW cm^{-2}. The best agreement with the experimental lineshape is found at these intensities when we used slightly longer pulses, that is, increasing each XUV pulse duration by 10%. We note that the pulses in

https://doi.org/10.1038/s41566-026-02024-9

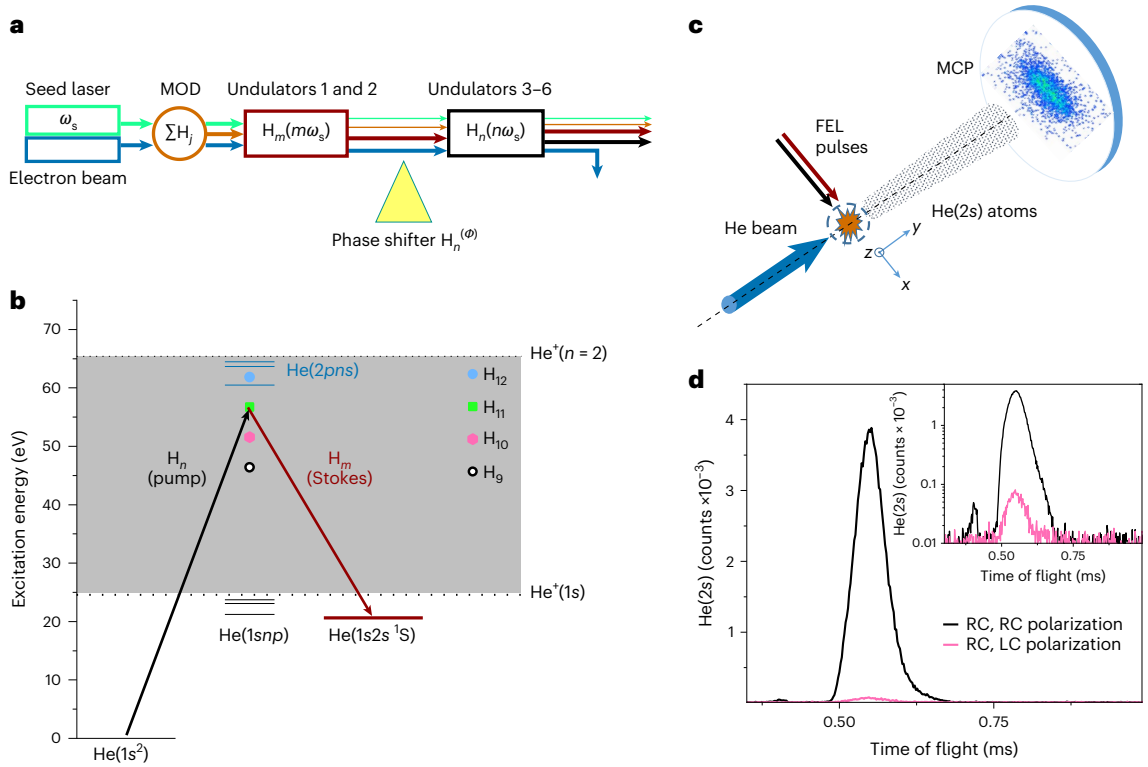


Fig. 1 | Scheme and experimental set-up for demonstrating the two-photon XUV stimulated Raman excitation of He. a, Schematic diagram of harmonic generation in the XUV. A seed laser beam with angular frequency ω_s is sent through a modulator (MOD) together with a high-energy electron beam. It induces a coherent energy modulation, which is then converted into a density modulation (bunching) at frequency ω_s and its integer harmonics H_j. Downstream undulators are set to support the coherent emission of the bunched beam to the desired harmonic. Dividing the undulators into two sets, tuned at harmonics H_n and H_m, enables the generation of 'pump' and 'Stokes' pulses, respectively. The phase shifter $H_n^{(\Phi)}$ shifts the phase Φ of harmonic H_n. **b**, Level diagram of He (singlet states) and scheme of stimulated Raman excitation of the metastable He(1s2s ^{1}S) state via pairs of harmonics. He(1snp) denotes the first states of the bound Rydberg series. The grey area depicts the continuum, which includes the autoionizing resonances He(2pns). **c**, Experimental set-up. We use a supersonic beam of He atoms, which is intersected by the two focused XUV pulses (Methods). Excited long-lived metastable He(1s2s ^{1}S) atoms, abbreviated as He(2s), travel within the atomic He beam towards the position-sensitive MCP detector, where they are detected after a travel time of about 500 µs. The electric field plates across the interaction region, which deflect ions and electrons perpendicular to the atomic beam in the z direction, are indicated by the dashed circle. **d**, Time-of-flight spectrum of He(2s) atoms excited, on Raman resonance, by the pair of circularly polarized harmonics (H_7, H_{11}) with intensities of 118 and 984 TW cm^{-2}, respectively. The black line denotes the He(2s) yield for the harmonics with the same helicity, that is, dipole-allowed excitation. The pink line shows the He(2s) yield for opposite helicities, that is, dipole-forbidden excitation. Inset: main diagram, but with the yield plotted on a logarithmic scale. RC, right circular; LC, left circular.

the calculation are Fourier-limited pulses, although this is not fully true for the XUV pulses generated at the FERMI facility.

To elucidate the intensity dependence of the He(2s) yield and of the lineshape of the resonance further, we carried out calculations for the H_7, H_{11} pair of harmonics over a broad range of pulse intensities. In Fig. 2c we display the final-state populations of the ground-state He(1s^2) and the final He(2s) state as a function of the intensity product $I_{H7} \times I_{H11}$. The laser frequencies were tuned to the Raman resonance. We recognize the nearly linear behaviour of the He(2s) yield for values of the intensity product of ≤10^4 TW^2 cm^{-4}. At the upper limit of linearity, He is substantially ionized, leaving a residual population of about 20% in the ground state. At higher intensities the He(2s) yield saturates and notably remains nearly constant at a population level of slightly below 1%. At the same time the ground-state population is completely depleted. Notably, the excited He(2s) population is shielded during the whole Raman process from being ionized, and can also be observed in the fully saturated regime. This is due to the fact that, at high intensities, it is produced at the beginning of the pulses, when there is still a high population of ground-state atoms and its ionization is much less than for ground-state atoms.

Furthermore, the calculations reveal that the Stark shift of the He(2s) resonance remains negligible up to an intensity product of about 10^5 TW^2 cm^{-4}. Only at even higher intensities does the resonance position shift slightly, although the resonance lineshape remains unaltered—see the left panel of Fig. 2d. The residual populations of He(1s^2) are displayed in the right panel of Fig. 2d. They reveal the characteristic Fano-like lineshape in the ground-state population[12] (curve γ), and show a slight change only at the highest intensity by exhibiting an additional minimum (curve δ).

Interfering stimulated Raman pathways

We recall that the phases of fields and dipole moments cancel in a simple coherent two-colour Raman transition and are not observable. The matrix element M for this transition, which is given in second-order perturbation theory explicitly in Supplementary Information, Section 4, can be written in the abbreviated form $M = |M|e^{-i\phi}$, where ϕ comprises all phases of the fields and the matrix element, e is Euler's number and i is the imaginary unit. The excitation cross-section, which is proportional to the square of the matrix element, $\sigma_{Raman} \propto |M|^2$, is independent of the phases, as expected.

If two coherent Raman pathways simultaneously excite the final state, even though the pathways proceed via two different continuum states, they are, in principle, indistinguishable and phases become observable. To show this, we emphasize in the abbreviated form of the

https://doi.org/10.1038/s41566-026-02024-9

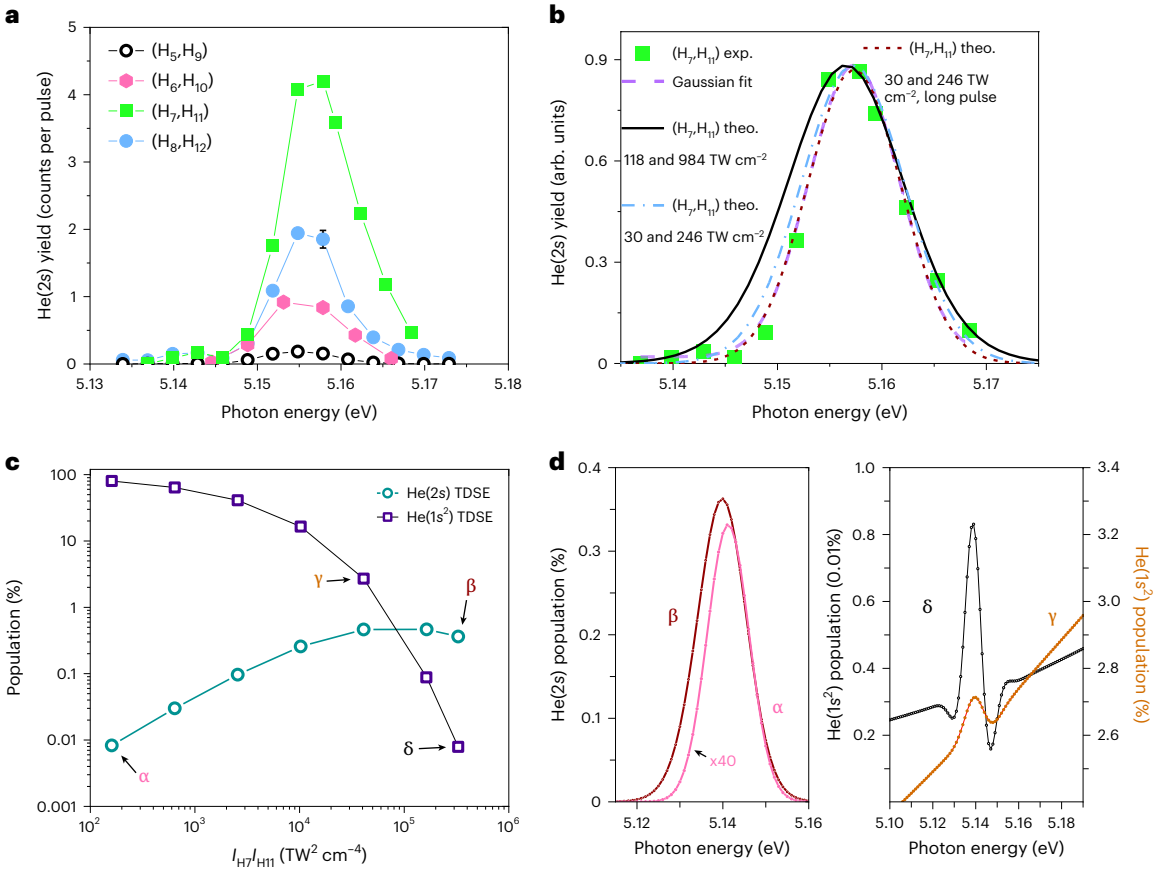


Fig. 2 | XUV stimulated Raman excitation spectra and theoretical analysis. **a**, Measurement of the Raman resonance for four harmonic pairs (m, n) at the maximum respective pulse energies generated: (5, 9) at 1.3 and 10 μJ (open black circles), (6, 10) at 20 μJ total energy (pink hexagons), (7, 11) at 12 and 40 μJ (blue circles) and (8, 12) at 11 and 30 μJ (green squares). The He(2s) yield is plotted as a function of the photon energy of the seed laser E_s. The black error bar denotes the standard deviation of the mean of three measurements, and represents the reproducibility. The statistical counting error of each data point is within the size of the data point. **b**, Comparison of the experimentally obtained (exp.) (H_7, H_{11}) Raman resonance with the theoretical (theo.) results. Calculations were performed with XUV pulse durations of 61 and 52 fs, respectively, at intensities of 118 and 984 TW cm^{-2} (black line) and 30 and 246 TW cm^{-2} (blue dot-dashed line). Results of the calculation with longer pulse durations (67 and 57 fs) and respective intensities of 30 and 246 TW cm^{-2} are shown by the dashed dark-red line. For the experimentally measured data, the measured He(2s) yield (green squares) is fitted with a Gaussian curve (violet dashed line). As the calculated resonance position deviates from the experimental one, we have shifted the theoretical data in energy accordingly (Methods). **c**, Calculated He(2s) population (open green circles) and He(1s^2) ground-state population (open violet squares) as a function of the intensity product of H_7 and H_{11}, at a fixed intensity ratio. α, β, γ and δ indicate the data points for which spectral distributions of the populations are plotted in **d**. **d**, Left: He(2s) population (curves α and β) as a function of the theoretical seed laser photon energy. Right: He(1s^2) population (curves γ and δ) as a function of the theoretical seed laser photon energy.

second transition matrix element, M', the phase Φ of one of the Stokes or pump fields explicitly, and comprise all other phases in ϕ', so that $M' = |M'|e^{-i\phi'}e^{-i\Phi}$. The cross-section then reads

$$\sigma_{\text{Raman}}^{\text{two-way}} \propto ||M|e^{-i\phi} + |M'|e^{-i\phi'}e^{-i}|^2 = |M|^2 + |M'|^2 + |M||M'|\cos(\Phi - (\phi - \phi')).$$

The cross-section $\sigma_{\text{Raman}}^{\text{two-way}}$ exhibits a cosine modulation as a function of the phase Φ of the field, shifted by the constant difference between the other phases of the two pathways.

With our experimental set-up, we were able to generate interfering Raman pathways and, as shown in Fig. 1a, we also had the capability to vary the phase of the harmonic that is amplified in the second undulator set. Owing to the nature of our excitation scheme, all pairs of harmonics with ($m = n - 4$, n) of a properly tuned seed laser drive a Raman resonance. If the intense Stokes laser photon of the main Raman pathway (harmonic H_m) is taken to serve as the pump photon of the second pathway (Fig. 3a), an additional weak harmonic H_l of harmonic order $l = m - 4$ provides the Stokes laser photon for the second pathway. Although the unamplified harmonic is rather weak, the total efficiency of the second pathway is boosted by the much larger cross-section for the second pair, including the weak lower harmonics (H_l, H_m), than for the pair of intense harmonics (H_m, H_n). The increasing Raman excitation cross-section involving lower harmonics photon energies is displayed in the Extended Data Fig. 1.

First, we experimentally demonstrated the interference of the (H_8, H_{12}) and (H_4, H_8) Raman pathways. In addition to the amplified harmonics (H_8, H_{12}) providing the first Raman pathway we used the unamplified harmonic H_4, which is typically present in the XUV spectrum at a 0.1% level of the total pulse energy, to form the second pathway (H_4, H_8). To observe the two-path Raman interference we used the phase shifter between the two undulator sets to vary the phase of H_{12} with respect to H_4 and H_8 (Fig. 1a). By scanning the phase, we found that the He(2s) yield varies periodically, as displayed in Fig. 3b, demonstrating the high degree of coherence deep in the XUV regime. We also show a theoretical TDSE calculation which confirms the experimental observation. The pulse parameters for the harmonics H_8 and H_{12} were taken from the experiment. The pulse energy of the spurious H_4 was taken to be 1/40 of 0.1% of the total pulse energy to match the visibility of the fringes. Calculating the He(2s) yields for the two pathways with these pulse parameters separately, we find the yield for the (H_4, H_8) transition to

https://doi.org/10.1038/s41566-026-02024-9

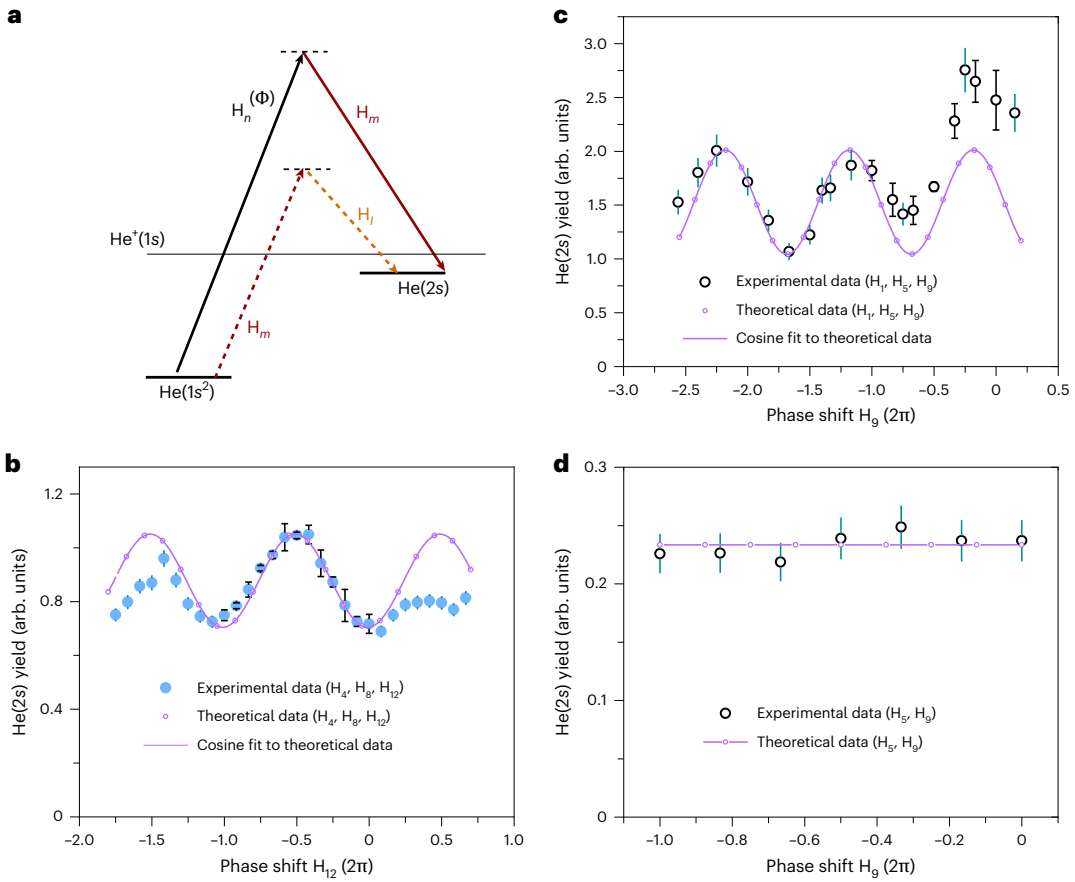


Fig. 3 | Interfering Raman pathways. a, Scheme for generating two interfering pathways. H_m and H_n ($n-m=4$) are the amplified harmonics (black and dark-red lines). H_l ($l=m-4$) is the unamplified harmonic or seed laser (orange dashed line). **b**, Interference of the pathways (H_8, H_{12}) and (H_4, H_8), where the measured He(2*s*) yield as a function of the phase shift of harmonic H_{12} is shown as the blue circles. The data points with black error bars, which indicate the standard deviation of the mean, are the mean values of repeated individual measurements (either two or three). All other data points stem from single measurements. The average values of the relative mean errors were taken to assign an estimated error to these data points (green error bars without caps). The results of a TDSE calculation using field strengths (0.1, 100 and 770 TW cm^{-2}) for the three harmonics (H_4, H_8 and H_{12}), respectively, are shown as open violet circles. The cosine fit to the theoretical data is shown via the violet line. **c**, Interference of the pathways (H_5, H_9) and (H_1, H_5). The measured He(2*s*) yield as a function of the phase shift of harmonic H_9 is shown as open black circles. The error bars are as defined in **b**. The results of a TDSE calculation using field strengths (0.72, 4.68 and 35.9 TW cm^{-2}) for the three harmonics (H_1, H_5 and H_9), respectively, as shown as open violet circles. The cosine fit to the theoretical data is shown as the violet line. **d**, Single pathway (H_5, H_9). The measured He(2*s*) yield as a function of the phase shift of harmonic H_9 is shown as open black circles. The data points stem from single individual measurements. The average values of the relative mean errors in **c** were taken to assign an estimated error to these data points (green error bars without caps). The results of a TDSE calculation using field strengths (4.68 and 35.9 TW cm^{-2}) for the two harmonics (H_5 and H_9), respectively, are shown as the open violet circles. The solid violet line acts as a guide to the eye.

be 1.8% of the (H_8, H_{12}) yield. Phase fluctuations, which possibly reduce the fringe visibility, are not considered. We note that we do not observe interference for the pair (H_7, H_{11}), indicating that in this configuration the amount of unamplified signal at the third harmonic is substantially suppressed and no second pathway (H_3, H_7) is established. To clearly demonstrate experimentally that interference indeed vanishes when one of the two pathways is blocked, we used another two pairs of harmonics, for which it was technically feasible to block one of the laser frequencies involved.

In this alternate approach, we take advantage of the fact that the seed laser radiation, H_1, is also present in the interaction region. Although the pulse energy is very low (on the order of 100 nJ) it can be used very efficiently together with harmonic H_5 to provide the second Raman pathway. As the photon energy of harmonic H_5 reaches only barely into the continuum above the first ionization threshold, the nonlinear Raman transition using the fundamental frequency as the Stokes photon shows by far the highest cross-section, as depicted in Extended Data Fig. 1. Moreover, it is technically easily feasible to block the fundamental radiation H_1 from reaching the interaction region by simply inserting an aluminium filter into the path of the FEL beam.

Together with the amplified harmonics (H_5, H_9) we now realized the two interfering pathways. Again, using the phase shifter between the two undulator sets, we varied the phase of harmonic H_9 with respect to harmonic H_5 and to the fundamental H_1. As the seed laser was sufficiently phase-stable, this, in turn, led to a controlled phase shift between the two interfering Raman pathways. This resulted in a similar periodic modulation as in the case investigated before (Fig. 3c), but with a higher fringe visibility of about 50%. When we inserted the aluminium filter, which also slightly reduced the intensities of harmonics H_5 and H_9, we no longer observed the modulation in the yield (Fig. 3d).

To analyse the data quantitatively, we calculated the interference with the experimental field strengths of the three pulses (H_1, H_5 and H_9). The result, which shows very good agreement with the experiment, is plotted in Fig. 3c. We note that we had to shift the theoretical results by a few degrees to match the experimental data due to the unknown absolute phase of the interference signal. The calculations revealed that, in this combination, the (H_1, H_5) contribution dominates, which is in accord with the fact that the cross-section for this combination is much larger than for the combination (H_5, H_9).

In conclusion, the successful demonstration of a coherent stimulated Raman excitation using two controllable XUV pulses and control of interfering Raman pathways opens a new and exciting avenue for applying phase-sensitive methods for coherent control measurements in the ionization continuum for atomic and molecular processes. Moreover, the outlook of steady FEL development aimed at two independently tunable coherent laser pulses will finally enable investigations into strong-field phase modulations in stimulated Raman excitation. This is particularly the case in the vicinity of autoionizing resonances, where dramatic Stark shifts along with strong lineshape alterations are theoretically expected (Supplementary Information, Section 5 and Supplementary Fig. 3), which could be perfectly studied using our experimental approach.

Online content

Any methods, additional references, Nature Portfolio reporting summaries, source data, extended data, supplementary information, acknowledgements, peer review information; details of author contributions and competing interests; and statements of data and code availability are available at https://doi.org/10.1038/s41566-026-02024-9.

References

1. McNeil, B. W. J. & Thompson, N. R. X-ray free-electron lasers. *Nat. Photonics* **4**, 814–821 https://doi.org/10.1038/nphoton.2010.239 (2010).
2. Maroju, P. K. et al. Attosecond coherent control of electronic wave packets in two-colour photoionization using a novel timing tool for seeded free-electron laser. *Nat. Photonics* **17**, 200–207 https://doi.org/10.1038/s41566-022-01127-3 (2023).
3. Guo, Z. et al. Experimental demonstration of attosecond pump-probe spectroscopy with an X-ray free-electron laser. *Nat. Photonics* **18**, 691–697 https://doi.org/10.1038/s41566-024-01419-w (2024).
4. Chergui, M., Beye, M., Mukamel, S., Svetina, C. & Masciovecchio, C. Progress and prospects in nonlinear extreme-ultraviolet and X-ray optics and spectroscopy. *Nat. Rev. Phys.* **5**, 578–596 https://doi.org/10.1038/s42254-023-00643-7 (2023).
5. Picón, A., Mompart, J. & Southworth, S. H. Stimulated Raman adiabatic passage with two-color x-ray pulses. *New J. Phys.* **17**, 083038 https://doi.org/10.1088/1367-2630/17/8/083038 (2015).
6. Kukura, P., McCamant, D. W. & Mathies, R. A. Femtosecond stimulated Raman spectroscopy. *Annu. Rev. Phys. Chem.* **58**, 461–488 https://doi.org/10.1146/annurev.physchem.58.032806.104456 (2007).
7. Prince, R. C., Frontiera, R. R. & Potma, E. O. Stimulated Raman scattering: from bulk to nano. *Chem. Rev.* **117**, 5070–5094 https://doi.org/10.1021/acs.chemrev.6b00545 (2017).
8. Bergmann, K., Theuer, H. & Shore, B. W. Coherent population transfer among quantum states of atoms and molecules. *Rev. Mod. Phys.* **70**, 1003–1025 https://doi.org/10.1103/RevModPhys.70.1003 (1998).
9. Vitanov, N. V., Rangelov, A. A., Shore, B. W. & Bergmann, K. Stimulated Raman adiabatic passage in physics, chemistry, and beyond. *Rev. Mod. Phys.* **89**, 015006 https://doi.org/10.1103/RevModPhys.89.015006 (2017).
10. Monroe, C. et al. Resolved-sideband Raman cooling of a bound atom to the 3D zero-point energy. *Phys. Rev. Lett.* **75**, 4011–4014 https://doi.org/10.1103/PhysRevLett.75.4011 (1995).
11. Kasevich, M. & Chu, S. Atomic interferometry using stimulated Raman transitions. *Phys. Rev. Lett.* **67**, 181–184 https://doi.org/10.1103/PhysRevLett.67.181 (1991).
12. Knight, P. L., Lauder, M. A. & Dalton, B. J. Laser-induced continuum structure. *Phys. Rep.* **190**, 1–61 https://doi.org/10.1016/0370-1573(90)90089-K (1990).
13. Nakajima, T., Elk, M., Zhang, J. & Lambropoulos, P. Population transfer through the continuum. *Phys. Rev. A* **50**, R913–R916 https://doi.org/10.1103/PhysRevA.50.R913 (1994).
14. Rangelov, A. A., Vitanov, N. V. & Arimondo, E. Stimulated Raman adiabatic passage into continuum. *Phys. Rev. A* **76**, 043414 https://doi.org/10.1103/PhysRevA.76.043414 (2007).
15. Boller, K.-J., Imamoğlu, A. & Harris, S. E. Observation of electromagnetically induced transparency. *Phys. Rev. Lett.* **66**, 2593–2596 https://doi.org/10.1103/PhysRevLett.66.2593 (1991).
16. Young, L. et al. Femtosecond electronic response of atoms to ultra-intense X-rays. *Nature* **466**, 56–61 https://doi.org/10.1038/nature09177 (2010).
17. Weninger, C. et al. Stimulated electronic X-ray Raman scattering. *Phys. Rev. Lett.* **111**, 233902 https://doi.org/10.1103/PhysRevLett.111.233902 (2013).
18. Li, K. et al. Super-resolution stimulated X-ray Raman spectroscopy. *Nature* **643**, 662–668 https://doi.org/10.1038/s41586-025-09214-5 (2025).
19. Eichmann, U. et al. Photon-recoil imaging: expanding the view of nonlinear x-ray physics. *Science* **369**, 1630–1633 https://doi.org/10.1126/science.abc2622 (2020).
20. O'Neal, J. T. et al. Electronic population transfer via impulsive stimulated x-ray Raman scattering with attosecond soft-x-ray pulses. *Phys. Rev. Lett.* **125**, 073203 https://doi.org/10.1103/PhysRevLett.125.073203 (2020).
21. Alexander, O. et al. Attosecond impulsive stimulated X-ray Raman scattering in liquid water. *Sci. Adv.* **10**, eadp0841 https://doi.org/10.1126/sciadv.adp0841 (2024).
22. Higley, D. J. et al. Stimulated resonant inelastic X-ray scattering in a solid. *Commun. Phys.* **5**, 83 https://doi.org/10.1038/s42005-022-00857-8 (2022).
23. Morillo-Candas, A. S. et al. Coherent nonlinear X-ray four-photon interaction with core-shell electrons. *Nature* **649**, 590–596 https://doi.org/10.1038/s41586-025-09911-1 (2026).
24. Li, X., McCurdy, C. W. & Haxton, D. J. Population transfer between valence states via autoionizing states using two-color ultrafast π pulses in XUV and the limitations of adiabatic passage. *Phys. Rev. A* **89**, 031404 https://doi.org/10.1103/PhysRevA.89.031404 (2014).
25. Greenman, L., Koch, C. P. & Whaley, K. B. Laser pulses for coherent XUV Raman excitation. *Phys. Rev. A* **92**, 013407 https://doi.org/10.1103/PhysRevA.92.013407 (2015).
26. Greenman, L., Whaley, K. B., Haxton, D. J. & McCurdy, C. W. Optimized pulses for Raman excitation through the continuum: verification using the multiconfigurational time-dependent Hartree–Fock method. *Phys. Rev. A* **96**, 013411 https://doi.org/10.1103/PhysRevA.96.013411 (2017).
27. Strelkov, V. V., Birulia, V. A. & Magunov, A. I. Method of XUV attosecond pulse characterization using two-photon resonant Raman-type transition. *New J. Phys.* **20**, 093025 https://doi.org/10.1088/1367-2630/aae101 (2018).
28. Moshammer, R. et al. Few-photon multiple ionization of Ne and Ar by strong free-electron-laser pulses. *Phys. Rev. Lett.* **98**, 203001 https://doi.org/10.1103/PhysRevLett.98.203001 (2007).
29. Fushitani, M. et al. Femtosecond two-photon Rabi oscillations in excited He driven by ultrashort intense laser fields. *Nat. Photonics* **10**, 102–105 https://doi.org/10.1038/nphoton.2015.228 (2016).
30. Nandi, S. et al. Observation of Rabi dynamics with a short-wavelength free-electron laser. *Nature* **608**, 488–493 https://doi.org/10.1038/s41586-022-04948-y (2022).
31. Nandi, S. et al. Generation of entanglement using a short-wavelength seeded free-electron laser. *Sci. Adv.* **10**, eado0668 https://doi.org/10.1126/sciadv.ado0668 (2024).
32. Bencivenga, F. et al. Four-wave mixing experiments with extreme ultraviolet transient gratings. *Nature* **520**, 205–208 https://doi.org/10.1038/nature14341 (2015).

33. Rottke, H. et al. Probing electron and hole colocalization by resonant four-wave mixing spectroscopy in the extreme ultraviolet. *Sci. Adv.* **8**, eabn5127 https://doi.org/10.1126/sciadv.abn5127 (2022).
34. Brumer, P. & Shapiro, M. Control of unimolecular reactions using coherent light. *Chem. Phys. Lett.* **126**, 541–546 https://doi.org/10.1016/S0009-2614(86)80171-3 (1986).
35. Prince, K. C. et al. Coherent control with a short-wavelength free-electron laser. *Nat. Photonics* **10**, 176–179 https://doi.org/10.1038/nphoton.2016.13 (2016).
36. Žitnik, M. et al. Interference of two-photon transitions induced by XUV light. *Optica* **9**, 692–700 https://doi.org/10.1364/OPTICA.447436 (2022).
37. Allaria, E. et al. Highly coherent and stable pulses from the FERMI seeded free-electron laser in the extreme ultraviolet. *Nat. Photonics* **6**, 699–704 https://doi.org/10.1038/nphoton.2012.233 (2012).
38. Kramida, A., Ralchenko, Y., Reader, J. & NIST ASD Team. *NIST Atomic Spectra Database (version 5.12)* https://physics.nist.gov/asd (National Institute of Standards and Technology, accessed 31 January 2026).
39. Cinquegrana, P. et al. The seed laser system of the FERMI free-electron laser: design, performance and near future upgrades. *High Power Laser Sci. Eng.* **9**, e61 https://doi.org/10.1017/hpl.2021.49 (2021).
40. Penent, F. et al. Observation of triplet doubly excited states in single photon excitation from ground state helium. *Phys. Rev. Lett.* **86**, 2758–2761 https://doi.org/10.1103/PhysRevLett.86.2758 (2001).
41. Žitnik, M. et al. High resolution multiphoton spectroscopy by a tunable free-electron-laser light. *Phys. Rev. Lett.* **113**, 193201 https://doi.org/10.1103/PhysRevLett.113.193201 (2014).
42. Allaria, E. et al. Control of the polarization of a vacuum-ultraviolet, high-gain, free-electron laser. *Phys. Rev. X* **4**, 041040 https://doi.org/10.1103/PhysRevX.4.041040 (2014).
43. Patchkovskii, S. & Muller, H. G. Simple, accurate, and efficient implementation of 1-electron atomic time-dependent Schrödinger equation in spherical coordinates. *Comput. Phys. Commun.* **199**, 153–169 https://doi.org/10.1016/j.cpc.2015.10.014 (2016).

Publisher's note Springer Nature remains neutral with regard to jurisdictional claims in published maps and institutional affiliations.

Open Access This article is licensed under a Creative Commons Attribution 4.0 International License, which permits use, sharing, adaptation, distribution and reproduction in any medium or format, as long as you give appropriate credit to the original author(s) and the source, provide a link to the Creative Commons licence, and indicate if changes were made. The images or other third party material in this article are included in the article's Creative Commons licence, unless indicated otherwise in a credit line to the material. If material is not included in the article's Creative Commons licence and your intended use is not permitted by statutory regulation or exceeds the permitted use, you will need to obtain permission directly from the copyright holder. To view a copy of this licence, visit http://creativecommons.org/licenses/by/4.0/.

© The Author(s) 2026

[1]Max Born Institute, Berlin, Germany. [2]Technische Universität Berlin, Berlin, Germany. [3]Department of Physics and Astronomy, Uppsala University, Uppsala, Sweden. [4]Institut für Physik, Universität Kassel, Kassel, Germany. [5]Elettra Sincrotrone Trieste, Trieste, Italy. [6]CNR - Istituto Officina dei Materiali (IOM), Trieste, Italy. [7]Institute of Condensed Matter and Nanosciences, Université catholique de Louvain, Louvain-la-Neuve, Belgium. [8]Present address: ASTeC, STFC UKRI Daresbury Laboratory and Cockcroft Institute, Daresbury Laboratory, Warrington, UK. [9]Present address: Institute of Chemical Sciences, Heriot-Watt University, Edinburgh, UK. [10]Present address: European XFEL GmbH, Schenefeld, Germany. ✉e-mail: eichmann@mbi-berlin.de

Methods

Experiments

We performed the experiments at the LDM (Low Density Matter) beamline of the FERMI facility of Elettra Sincrotrone Trieste[44]. We use the Even–Lavie supersonic source, which we operate at a stagnation pressure of ~5 bar of He gas, to provide the He beam. As displayed schematically in Fig. 1a, we produce the two XUV FEL pulses by generating a pair of harmonics with orders $(n-4, n)$ of the seed laser wavelength in the two undulator sets, respectively. The amplification of the two harmonics entails an intrinsic time delay between the two pulses. As a result, in the given undulator configuration the pump pulse (H_n) trails the Stokes pulse (H_m) pulse by 15 fs. The pulse duration (at FWHM) is between 50 and 100 fs, depending on the harmonic order[45]. At the seed laser photon energy of 5.154 eV, we achieve maximum pulse energies of 10 and 1.3 µJ, a total of 20 µJ, 40 and 12 µJ, and 30 and 11 µJ for the harmonic pairs (H_5, H_9), (H_6, H_{10}), (H_7, H_{11}) and (H_8, H_{12}) respectively. The FEL beam is focused using a Kirkpatrick–Baez active optics system[46]. The two foci of the two harmonics are separated by 2 mm as a result of their different places of origin. As the Rayleigh length of each focused harmonic beam exceeds the longitudinal separation of the two foci, there is an effective overlap of the two harmonic beams between the two foci with an effective beam waist of about $w_0 \propto 10$ µm. The atomic beam is adjusted to pass through this area. Besides the longitudinal offset of the two harmonic beams, there may also be a displacement of a few micrometres, which potentially causes the effective intensity product of the two XUV pulses to decrease substantially. This displacement has not been quantitatively characterized. Across the interaction region a small static field is present, which pushes either electrons or ions, depending on the polarity, towards a velocity-mapping-imaging detector, which was used for monitoring purposes. We detect metastable He atoms using a position-sensitive MCP detector (RoentDek, Delay Line Detector), which is installed about 1 m behind the interaction region (Fig. 1c).

Numerical calculations

We solved the TDSE in the velocity gauge and dipole approximation for an effective one-electron potential (Supplementary Information, Section 3). This single-electron approach is justified, as the photon energies of all pairs of harmonics are sufficiently off-resonance from autoionizing states in the continuum. The approach naturally includes all orders of nonlinearity that are associated with the high laser field strength involved. For the singlet manifold we used a model potential for He in the following form (atomic units):

$$v(r) = -\frac{1}{r} - \frac{0.6731\mathrm{e}^{-4r}}{r} - \frac{0.3269\mathrm{e}^{-0.4r}}{r} + 0.1056\mathrm{e}^{-0.6618r}r, \qquad (1)$$

where r is the electron-nucleus distance and $v(r)$ is the model interaction potential. The potential has been optimized to accurately reproduce the energies of the $1s^2\,{}^1\mathrm{S}$, $1s2s\,{}^1\mathrm{S}$, $1s2p\,{}^1\mathrm{P}^o$ and $1s3d\,{}^1\mathrm{D}$ states of the He atom[38] as well as the singlet Rydberg progression of the ground-state He^+ ion. In the majority of the cases, the calculated excitation energies match the literature values better than 0.1% (Supplementary Table 1). The energy difference (Δ) of the calculated excitation energy of the metastable He(2s) state from the literature value [38] is slightly higher, that is, Δ = −53 meV.

Calculations used a uniform radial grid extending to 90 bohr (grid spacing 0.1 bohr), with the last 32.78 bohr covered by a transmission-free absorbing boundary[47]. Spherical expansion with a maximum angular momentum (L_{max}) of 5 was used for the angular part. Time propagation used a fixed, uniform time step of 0.02 atomic units. The computer code is described in ref. 43 and is available at https://github.com/MBI-Theory/scid-tdse.

We performed the calculations with either circularly or linearly polarized XUV pulses. Using either parallel linear polarization or the same handedness of circular polarization for the XUV pulses led to the same results. This is in line with the fact that the geometrical factors in the matrix elements are the same in both cases. The computing time, however, was strongly reduced for linear polarization.

Data availability

All data used in the Article are available via Zenodo at https://doi.org/10.5281/zenodo.22132955 (ref. 48).

References

44. Svetina, C. et al. The low density matter (LDM) beamline at FERMI: optical layout and first commissioning. *J. Synchrotron Radiat.* **22**, 538–543 https://doi.org/10.1107/S1600577515005743 (2015).
45. Finetti, P. et al. Pulse duration of seeded free-electron lasers. *Phys. Rev. X* **7**, 021043 https://doi.org/10.1103/PhysRevX.7.021043 (2017).
46. Raimondi, L. et al. Kirkpatrick–Baez active optics system at FERMI: system performance analysis. *J. Synchrotron Radiat.* **26**, 1462–1472 https://doi.org/10.1107/S1600577519007938 (2019).
47. Manolopoulos, D. E. Derivation and reflection properties of a transmission-free absorbing potential. *J. Chem. Phys.* **117**, 9552–9559 https://doi.org/10.1063/1.1517042 (2002).
48. Eichmann, U. et al. Phase control of interfering stimulated Raman pathways in the XUV regime. *Zenodo* https://doi.org/10.5281/zenodo.22132955 (2026).

Acknowledgements

We thank C. Spezzani and M. Bonanomi for their support of the experiment. The project received funding from the European Union's Horizon 2020 research and innovation programme under grant agreement no. 871124 Laserlab-Europe (PID 21874). J.M. gratefully acknowledges funding from the European Research Council (ERC) under the EXCELLENT SCIENCE – European Research Council (ERC) programme within a Consolidator Grant (CoG agreement 101003142, https://doi.org/10.3030/101003142) and from the DFG within a Heisenberg professorship (project 470414645). J.-E.R. acknowledges financial support from the Swedish Research Council (VR project no. 2021-04017) and the Carl Trygger Foundation. M.G. acknowledges support from the Fonds de la Recherche Scientifique under IISN grant no. 4.4504.10. The funders had no role in the study design, data collection and analysis, decision to publish or preparation of the manuscript.

Author contributions

U.E. conceived and coordinated the study. U.E., S.C., S.P., J.-E.R., J.S., J.M., C.C., M.D.F., N.P., O.P. and M.G. performed the experiments. E.A., A.B., M.M., G.P. and A.S. prepared, optimized and characterized the two-colour mode operation of the FERMI FEL. U.E. analysed the data and performed the numerical calculations together with S.P. The paper was written by U.E., together with S.P., J.-E.R., J.M. and M.G. with input from J.S., C.C., M.D.F., M.G., E.A., A.B., M.M. and S.E.

Funding

Open access funding provided by Max-Born-Institut für Nichtlineare Optik und Kurzzeitspektroskopie (MBI) im Forschungsverbund Berlin e.V.

Competing interests

The authors declare no competing interests.

Additional information

Extended data is available for this paper at https://doi.org/10.1038/s41566-026-02024-9.

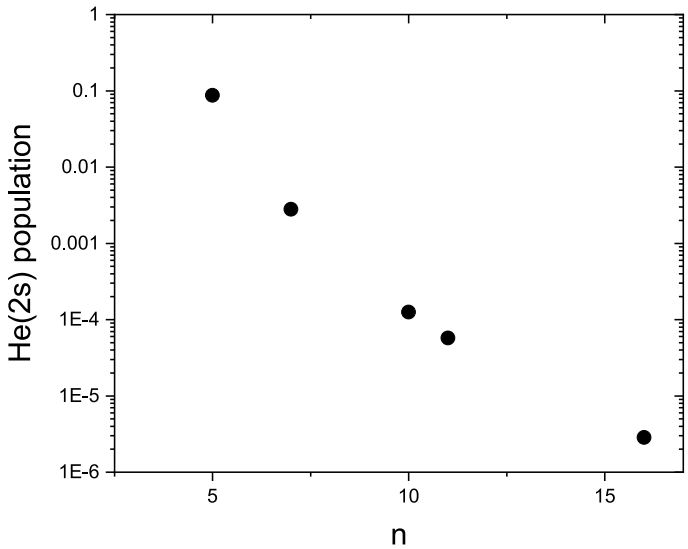
Supplementary information The online version contains supplementary material available at https://doi.org/10.1038/s41566-026-02024-9.

Correspondence and requests for materials should be addressed to Ulli Eichmann.

Peer review information *Nature Photonics* thanks Jasper J. van Thor and the other, anonymous, reviewer(s) for their contribution to the peer review of this work. Peer reviewer reports are available.

Reprints and permissions information is available at www.nature.com/reprints.

https://doi.org/10.1038/s41566-026-02024-9



Extended Data Fig. 1 | Calculated stimulated Raman excited He(2s) population as a function of the harmonic order n for pairs of harmonics (H_{n-4}, H_n). The pulse durations for both harmonics were 100 fs, and the intensities of the harmonics were I = 0.72TW cm^{-2} for harmonics H_{n-4} and I = 21.6TWcm^{-2} for harmonics H_n.